Chapter 3

S K-edge XAS Studies of the Effect of DNA Binding on the [4Fe4S] Site in Endo III and MutY

Adapted from: Ha, Y.; Arnold, A.R.; Nuñez, N.N.; Bartels, P.L.; Zhou, A.; David, S.S.; Barton, J.K.; Hedman, B.; Hodgson, K.O.; Solomon, E.I. Sulfur K-Edge XAS Studies of the Effect of DNA Binding on the [Fe_4S_4] Site in EndoIII and MutY. *J. Am. Chem. Soc.* **2017**, *139*, 11434 – 11442.

Y. Ha performed all XAS experiments and DFT analysis. A. Arnold, N. Nuñez, and A. Zhou purified DNA and proteins. P. Bartels performed UV-visible, CD, and EPR spectroscopy.

Introduction

Iron-sulfur clusters occur in a wide range of proteins with roles in electron transfer, catalysis, and regulation (*1*). Those involved in electron transfer are the rubredoxins and ferredoxins. Rubredoxin contains a mononuclear iron center with thiolate ligands, while ferredoxins contain multinuclear iron-sulfide clusters which includes [2Fe2S], [3Fe4S], and [4Fe4S] sites (*2*). The [Fe_4S_4] proteins can be further divided into two categories: the low-potential ferredoxins (Fd), which utilize the $[4Fe4S]^{2+/1+}$ redox couple with a potential as low as -600 mV, and high potential iron proteins (HiPIP), which have an $[4Fe4S]^{3+/2+}$ redox couple with a reduction potential as high as +350 mV (*1*). From X-ray crystallography (*3*), Extended X-Ray Absorption Fine Structure (EXAFS) (*4*) and resonance Raman (*5*) spectroscopic results, the $[4Fe4S]^{2+}$ sites in the Fds and HiPIPs are almost identical. They have similar bond distances and angles, as well as similar vibrational modes. The major difference is in their protein environments. The [4Fe4S] site in Fd is solvent exposed while this cluster in HiPIP is buried (*6*). Lyophilization of Fd and unfolding of HiPIP lead to significant changes in their S K-edge XAS spectra, showing that the H-bonds from solvent water change the Fe-S bond covalency (*7*). The higher covalency in HiPIP stabilizes the oxidized state over the reduced state, and this significantly contributes to their [4Fe4S] clusters utilizing different redox couples from Fd (*1*). The $[4Fe4S]^{2+}$ in Fd is less covalent and activated toward reduction, while the cluster in HiPIP is more covalent, and thus tuned toward oxidation.

Endonuclease III (EndoIII) and MutY are DNA glycosylases present in bacteria to humans that excise oxidized bases or their mispaired partners as initiating events in the Base Excision Repair (BER) pathway. Specifically, Endo III removes oxidized pyrimidines while MutY removes adenine from A:oxoG mispairs (where oxoG = 8-oxo-7,8-dihydroguanine) (*8, 9*).

The importance of these enzymes is highlighted by the correlation of inherited defects in human MutY (MUTYH) and early onset colorectal cancer, referred to as MUTYH-associated polyposis (MAP) (*10*). EndoIII and MutY both contain a $[4Fe4S]^{2+}$ cluster, which is redox inactive in solution in the absence of DNA (*11*). The $[4Fe4S]^{2+}$ cluster in these enzymes has been shown to be essential for substrate binding and catalysis, but, at least in the case of MutY, it is not required for global structural integrity of the enzyme (*9*). However, electrochemical experiments carried out with EndoIII and MutY on DNA-modified gold electrodes showed reversible redox signals at potentials ranging from 60 to 95 mV versus NHE, suggesting that DNA binding is able to activate these proteins for redox activity (*8*). A role for DNA in activating the cluster for redox activity was confirmed by electrochemistry on highly oriented pyrolytic graphite (HOPG) electrodes in the presence and absence of DNA; these experiments revealed that upon binding to DNA, the reduction potential of the $[4Fe4S]^{3+/2+}$ couple in EndoIII shifted ~ -200 mV into the physiological range and corresponding to a significantly increased DNA binding affinity of the oxidized form of the protein (*12, 13*). From electrochemical and *in vivo* experiments, a model has been proposed in which long-distance DNA-mediated electron transfer between two [4Fe4S] proteins with similar DNA-bound redox potentials facilitates the

search for damage across a vase genome (*8, 14-15*). If there is no DNA damage between the two binding sites, the charge transfer can proceed efficiently, and one of the DNA-bound proteins is reduced, thus its affinity for DNA is decreased. This protein can then dissociate and diffuse to another region of the genome. However, if there is a mismatch or lesion that disrupts the π-stacking of DNA, charge transfer will be attenuated and both proteins would remain bound to the DNA in the vicinity of the lesion. While the CT signaling model has been strongly supported in numerous studies, the cause of the large DNA-induced potential shift that makes such a damage search possible has remained puzzling. Electrostatic effects remain the most likely explanation, given that no significant structural changes are apparent between the free and DNA-bound forms of EndoIII and MutY. Unfortunately, the electrochemical techniques used in earlier work cannot reveal the fundamental molecular-scale changes involved, making an alternative approach necessary to elucidate these details.

S K-edge X-ray Absorption Spectroscopy (XAS) has been developed and applied to experimentally determine the covalency (α^2) of sulfur-metal bonds (i.e., the amount of S 3p character mixed into the metal 3d antibonding (Ψ^*) valence orbitals: $\Psi^* = \sqrt{1-\alpha^2}M_{3d} - \alpha S_{3p}$) (*16*). The S 1s orbital is localized on the S atom and the S 1s → S 3p transition is electric dipole allowed, thus the intensity of the 1s →Ψ^* pre-edge transition reflects the covalency of this bond. The energy of the pre-edge transition reflects the energy of the unoccupied or partially occupied Fe d-orbitals, which depends on the effective nuclear charge (Z_{eff}) of the metal and the nature of the ligand field (*16*). The pre-edge transition energy also depends on the charge of the S; sulfide

has a lower Z_{eff} than thiolate, thus the sulfide donor orbitals are at higher energy than those of the thiolate, and their associated S 1s $\rightarrow \Psi^*$ pre-edge transitions are at lower energy (*16*).

The intensity of a pre-edge peak D_0 is given by

$$D_0 = \sum c\alpha^2 \left| \langle S_{1s} | r | S_{3p} \rangle \right|^2 = \frac{\alpha^2 h}{3N} I_s \qquad (1)$$

where c is a constant, r is the dipole operator, α^2 is the bond covalency (i.e., sulfur p character mixed into the metal d orbitals), *N* is the total number of sulfurs bound to the metal, *h* is the total number of d electron holes, and I_s is the S 1s $\rightarrow$ 3p electric dipole integral, which is also dependent on the Z_{eff} of the S ligand and has been experimentally determined for thiolate and sulfide ligands in previous work (*17*). Our previous XAS studies on $[Fe_4S_4]$ sites showed that the contributions of thiolate and sulfide can be distinguished at the pre-edge, with the μ_3-sulfide pre-edge ~0.7 eV lower than the thiolate (*6, 18*). Quantitatively, for the [4(RS)4Fe4S] clusters, there are nine α holes and nine β holes (i.e., unoccupied valence orbitals), which have mainly Fe 3d and S 3p character (*6*); thus, the maximum covalency possible is 1800%. In particular, one unit of sulfide intensity corresponds to 30.6% S character per Fe-S bond, while 1 unit of thiolate corresponds to 70.8% S character in unoccupied valence orbitals. This difference reflects the different number of bonds to Fe (3 from sulfides and 1 from thiolate) and the difference in dipole integral due to the Z_{eff} of sulfide relative to thiolate S (6.54 vs 8.47) (*17*). Note that only the sulfur atoms bound to the iron contribute to the pre-edge feature in the XAS spectra, while all sulfur atoms including the free Cys and Met residues contribute to the edge. Thus, the pre-edge

intensity directly reflects the covalency of the thiolate-Fe and bridging sulfide-Fe bonds, but the edge normalization must be corrected for the total number of sulfurs in the protein.

The total pre-edge intensity, and therefore S covalency, in HiPIP is significantly higher than in Fd. The pre-edge intensity in a relevant alkyl thiolate [4Fe4S] model complex is even slightly higher than in HiPIP (*7*). Importantly, there is a direct correlation between the total S covalency and the redox potential of the [4Fe4S] clusters, with an increase of 1% of total S covalency corresponding to ~3.3 mV decrease in redox potential (*7*), which reflects the fact that higher covalency stabilizes the oxidized over the reduced state of the [4Fe4S] cluster. With respect to DNA repair proteins, the power of S K-edge XAS to monitor changes in [4Fe4S] cluster covalency under different conditions and to correlate these changes to redox potential results in an ideal method to elucidate the details of the DNA-induced potential shift at a molecular level.

In the present study, S K-edge XAS is applied to experimentally measure the Fe-S bond covalency of the [4Fe4S] clusters in EndoIII and MutY, both in the absence of and bound to DNA, and with and without solvent water. The effect of DNA binding on the S K-edge intensity and hence covalency is correlated to the reduction potential of the cluster according to a relationship defined in previous XAS studies on [4Fe4S] clusters (*7*) and is in agreement with the electrochemically observed reduction potential decrease upon DNA binding (*12*). The solvent effect is compared to those previously observed for Fd (*7*) and for the HiPIP proteins in this study. This work provides direct molecular evidence for the proposal that the negative charge of bound DNA tunes the potential of [4Fe4S] clusters and shows that this involves a change in the

covalency of the cluster that enables the $[4Fe4S]^{3+/2+}$ redox couple when EndoIII (and MutY) are bound to DNA.

Materials and Methods

Expression and Purification of EndoIII

WT *E. coli* EndoIII was overexpressed in BL21star-(DE3)pLysS cells containing a pET11-ubiquitin-His_6-*nth* construct and purified as detailed previously (*19*), with the exception that the final buffer contained 10% glycerol, rather than 20% glycerol (20 mM sodium phosphate, pH 7.5, 0.5 mM EDTA, 150 mM NaCl, 10% glycerol, Buffer A). EndoIII is less stable in the absence of glycerol; therefore glycerol was not removed until the day of sample preparation. Glycerol was removed from half the volume of protein solution using HiPrep 26/10 desalting column (GE Healthcare) equilibrated with Buffer A lacking glycerol. Next, the protein solutions either containing 10% glycerol or no glycerol were separately concentrated first with 10,000 MWCO (molecular weight cutoff) Amicon Ultra 15 mL centrifugation filter units (Millipore) and then with 10,000 MWCO Amicon Ultra 0.5 mL centrifugation filter units (Millipore) until the protein solutions were very dark colored, to approximately 300 μL each if using an entire protein preparation from 6 L of bacterial culture.

Expression and Purification of MutY

WT MutY was expressed as an N-terminal fusion with MBP (maltose binding protein) to increase the solubility at the concentrations needed for XAS experiments. Of note, the MBP tag has additional Met residues that can complicate XAS analysis. The MBP-MutY protein was overexpressed in BL21 DE3 competent cells and purified as detailed previously (*13*), with the following modification. Pelleted cells from overexpression were re-suspended in resuspension buffer (20 mM sodium phosphate, pH 7.5, 200 mM NaCl, 1mM EDTA, 10 % glycerol, 1 mM PMSF), sonicated on ice and centrifuged at 12,000 RPM for 15 minutes. The supernatant was saved in a conical tube on ice, and the pellet was re-suspended and underwent a repeat of

sonification and centrifugation. The supernatant was batch bound to amylose resin (New England BioLabs) for one hour, poured over a PD10 column and washed with amylose wash buffer (20 mM sodium phosphate, pH 7.5, 200 mM NaCl, 1mM EDTA) and eluted in amylose elutant buffer (20 mM sodium phosphate, pH 7.5, 200 mM NaCl, 1 mM EDTA, 10 mM maltose). The elutant was concentrated using an ultrafiltration cell with a 10,000 MWCO filter with stirring at 4oC. Protein was then diluted 10-fold in heparin buffer A (20 mM sodium phosphate, pH 7.5, 1 mM EDTA, 5% glycerol). The sample was applied to a Pharmacia Hi-trap heparin column on an AKTApurifier FPLC system, and eluted using a 10% linear gradient in heparin buffer A to 100% heparin buffer B (20 mM sodium phosphate, pH 7.5, 1 mM EDTA, 5 % glycerol, and 1 M NaCl). Fractions corresponding to MBP-MutY were combined and concentrated using an ultrafiltration cell with a 10,000 MWCO filter with stirring at 4 ^{o}C, to approximately 10mL. Purity of MBP-MutY samples was confirmed via 12% sodium dodecyl sulfate (SDS) PAGE stained with SYPRO orange and 7.5% acetic acid.

DNA Preparation

DNA strands for EndoIII studies were purchased from Integrated DNA Technologies (a 20-mer mixed sequence strand: 5′-GTGAGCTAACGTGTCAGTAC-3′ and its complement). DNA strands (5 μmol) were resuspended in MilliQ water (200 μL), and purified by ethanol precipitation. The purified strands were resuspended in Buffer A or Buffer A lacking glycerol and quantified based on calculated ε_{260} values for the strands (Integrated DNA Technologies) of 197,800 $M^{-1}cm^{-1}$ for the 20-mer strand and 190,200 $M^{-1}cm^{-1}$ for its complement. Annealing of the strands in either Buffer A or Buffer A without glycerol was accomplished by combining equimolar amounts of the single-stranded DNAs, heating at 90°C for 5 minutes, and slowly cooling to room temperature.

DNA strands for MutY studies containing oxoG (8-oxo-guanine) or FA (2'-fluoro-adenine) were synthesized at the University of Utah DNA and Peptide Synthesis Core Facility and unmodified strands were ordered from Integrated DNA Technologies. The following DNA duplexes were used:

15-mer: 5′ -GGA GCC AXG AGC TCC-3

15-mer Complement: 3′ -CCT CGG TYC TCG AGG-5′

30-mer: 5′ -CGA TCA TGG AGC CAC XAG CTC CCG TTA CAG-3′

30-mer Complement: 3′ -GCT AGT ACC TCG GTG YTC GAG GGC AAT GTC-5'

X = G or oxoG and Y = C, FA, or A

Oligonucleotides containing the central oxoG or FA were deprotected and cleaved from the column by incubation in NH_4OH, with the addition of 2-mercaptoethanol to oxoG samples to prevent oxidation. The cleaved DNA substrates were dissolved in H_2O, filtered with a 0.2 μm filter, and HPLC purified using a Beckman Gold Nouveau system with a Waters AP1DEAE 8HR column with a 10-100% gradient of 90:10 H2O/acetonitrile with 2 M NH_4Ac. Isolated fractions were lyophilized down and de-salted with a SEP-PAK C18 column, and DNA integrity was confirmed using MALDI-MS. All DNA substrates were stored dried in the -20^{o}C freezer prior to annealing to the complement strand.

XAS Sample Preparation

To prepare the EndoIII XAS samples, concentrated solutions of EndoIII protein were mixed with the DNA duplex at a ratio of 1 mol EndoIII: 20 mol base-pairs DNA. An equivalent volume of buffer was added to EndoIII alone solutions so that identical EndoIII concentrations were obtained both with and without DNA. Mixtures were allowed to incubate on wet ice for 30 minutes to allow for binding before freezing in liquid nitrogen. No glycerol samples were lyophilized. Both samples were placed on dry ice and sent to Stanford University for measurement. To confirm that lyophilized protein was not irreversibly altered by treatment, UV-visible and circular dichroism (CD) spectra were taken of untreated and redissolved samples.

To prepare the MutY XAS samples, purified MBP-MUTY samples were buffer exchanged in concentration buffer, with the final buffer composed of 20 mM sodium phosphate, pH 7.5, 150 mM NaCl, 1mM EDTA, 10% glycerol for samples to remain in buffer, or MBP-MutY concentration buffer lacking glycerol for samples to be lyophilized for XAS. The sample was concentrated to a final concentration of 1.2 mM. 125 uL of the purified MBP-MutY is incubated with 25uL of the 6mM annealed DNA duplex (see DNA contexts below) at 25 ^{o}C for 30 minutes to afford a final concentration of 1mM protein and DNA. Following lyophilization or immediately for the buffer samples, they were snap frozen in liquid nitrogen, stored in the -80 ^{o}C or dry ice, and thawed on ice just prior to XAS experiments. Purity of MBP-MutY samples was confirmed via 12 % SDS page stained with SYPRO orange and 7.5 % acetic acid. The [4Fe4S] cluster loading was determined using the UV-visible absorbance at 410 nm (ε_{410} = 17,000 $M^{-1}cm^{-1}$) and at 280 nm (ε_{280} = 143,240 $M^{-1}cm^{-1}$); samples were typically 65-75% loaded with cluster.

S K-edge XAS

Sulfur K-edge XAS data were measured at the Stanford Synchrotron Radiation Lightsource on the unfocussed 20-pole, 2.0-Tesla wiggler Beam Line 4-3, under SPEAR3 storage ring parameters of 3 GeV and 500 mA. A Ni-coated, flat, bent pre-monochromator mirror was used for harmonic rejection and vertical collimation. A Si(111) double crystal monochromator was used for energy selection. The energy calibration, data reduction, and error analysis follow the methods described in reference (*20*). Solid samples were ground into a fine powder and dispersed as thinly as possible on Kapton tape to minimize potential self-absorption effects. The solution samples were loaded into 50μL teflon cells, with Kapton tape as the back window, and 6 μm-thick, sulfur-free polypropylene film as front window. A shutter was inserted automatically during each monochromator move to minimize photoreduction. The photon energy was calibrated to the maximum of the first pre-edge feature of $Na_2S_2O_3 \cdot 5H_2O$ at 2472.02 eV. At least three scans were measured for each sample to ensure reproducibility. Raw data were calibrated and averaged using MAVE in the EXAFSPAK package (*21*). Using the PySpline program (*22*), the background was removed from all spectra by fitting a second-order polynomial to the pre-edge region and subtracting this from the entire spectrum. Normalization of the data was accomplished by fitting a straight line to the post-edge region and normalizing the edge jump to 1.0 at 2490.0 eV. The error from background subtraction and normalization is less than 3%. Intensities of the pre-edge features were quantified by fitting the data with pseudo-Voigt line shapes with a fixed Lorentzian to Gaussian ratio of 1:1, using the EDG_FIT program (*21*). Pre-edge energies and widths of single peaks were locked based on the previously published results on $[Fe_4S_4]$ models and proteins (*6*). The error from the fitting procedure is less than 3%. The fitted sulfide and thiolate intensities were converted to %S 3p character according to ref *17*.

Note that all the perturbations (lyophilization, mixing with DNA, and the combination) on EndoIII and MutY were done on aliquots of the same protein sample. This means that all the data on each protein presented in this study have the same loading ratio; thus, the differences observed upon DNA binding and lyophilization are independent of the loading.

DFT calculations

DFT calculations with broken symmetry spin polarization were performed using Gaussian 09 (*23*), with the pure functional BP86, and with 6-311G(d) basis sets on Fe and S, and 6-31G(d) basis sets on C and H. This functional and basis set were chosen to be consistent with previous studies (*7*). The α-carbons of the 4 Cys ligands were fixed to their crystal structure positions (*24*) during geometry optimizations. To qualitatively evaluate the electrostatic effect of DNA binding, a point charge was placed at 5 Å from either a sulfide or a thiolate S atom in the [4Fe4S] cluster, and the electronic structure was reoptimized.

Iron Quantification

To measure the extinction coefficient at 410 nm for two EndoIII mutants, Y205H and K208E, we followed an iron quantification protocol described in ref. *25*. Briefly, 100-150 μM EndoIII in storage buffer (20 mM sodium phosphate, pH 7.5, 150 mM NaCl, 0.5 mM EDTA) was denatured by addition of 125 μL 2 M HCl and precipitated with 125 μL 20% w/v TCA in water. Samples were spun down at 16000 x g (20 minutes), and the supernatant was collected and diluted in 250 μL saturated NaAc. Free iron was then reduced to the 2+ oxidation state with 6 μL thiolglycolic acid immediately prior to chelation with 50 μL 2,2′-bipyridine (0.4% w/v in an aqueous solution of 5% v/v acetic acid) to form $[Fe(bpy)_3]^{2+}$. Finally, iron was quantified by measuring absorbance at 522 nm using an extinction coefficient of 8789 $M^{-1}cm^{-1}$.

UV-visible Spectroscopy with and without DNA

To see if changes to the cluster environment could be observed at lower energies, the effect of DNA on the cluster environment in WT EndoIII and the mutants E200K, Y205H, and K208E was assessed by UV-visible spectroscopy. 10 μM EndoIII (by cluster) was prepared either alone or with equimolar (by duplex) DNA of the same sequence used for XAS experiments, and incubated on ice for 30 minutes prior to measurement. Spectra were compared following subtraction of a sample containing only DNA.

EPR Spectroscopy

The stability of EndoIII mutants was assessed using continuous wave X-band EPR spectroscopy at 10 K. All samples were prepared anaerobically in a glove bag under a 95% nitrogen, 5% hydrogen atmosphere. EndoIII (WT, Y82A, E200K, Y205H, or K208E) was diluted to 20 μM in degassed storage buffer (20 mM potassium phosphate, pH 7.5, 150 mM KCl, 0.5 mM EDTA) and either added directly to an EPR tube or first treated with 0.5, 1, 3, 5, or 10-fold molar excess of $K_3Fe(CN)_6$ to oxidize the cluster. Oxidized samples were frozen in liquid nitrogen as soon as possible following treatment. Spectra were taken at 12.88 mW microwave power, 2 G modulation amplitude, and 5.02 x 103 receiver gain. All samples were scanned 3 times, and a buffer background was subtracted from each. The lack of $K_3Fe(CN)_6$ contribution to the signal was confirmed with a sample containing only oxidant and buffer.

Results

S K-Edge XAS of EndoIII in the Absence and Presence of DNA

Sulfur K-edge XAS spectra of EndoIII in the absence and presence of a 20-mer mixed sequence DNA duplex (5′-GTGAGCTAACGTGTCAGTAC-3′ and its complement) at a ratio of 1 mol protein to 20 mol base-pairs were measured in both solution and lyophilized forms. UV-visible and CD spectra were taken of EndoIII before lyophilization and once redissolved post-treatment (Figure 3.1). Both spectra were indistinguishable, confirming that lyophilization does not affect cluster integrity or global protein folding. Protein concentrations at 1 mM or greater were used for high quality XAS data. Although highly concentrated, the protein shows no evidence of aggregation, and no changes are observed in UV-visible spectra or enzymatic activity levels of protein diluted from similarly concentrated stocks. Equal concentrations of EndoIII were compared without and with the DNA 20-mer. The data were first normalized to one sulfur, then corrected for non-bonding sulfur atoms (six in EndoIII) and the iron-sulfur cluster loading ratio, calculated as described in Materials and Methods. Cluster loading ratios for EndoIIII were 70% or greater. The spectra were then multiplied by 8 to evaluate the total contribution of four sulfide and four thiolate sulfur atoms.

The normalized S-K edge XAS spectra of the pre-edge region and the background (rising edge) subtracted spectral fits are shown in Figure 3.2. The energies and intensities obtained from the fits included in Figure 3.2 are given in Table 3.1. The peak assignments and the pre-edge shapes used in these fits are based on our previous results on [4Fe4S] clusters (*6, 7*). All pre-edge

spectra have two major features. The lower energy feature at ~2470.2 eV is due to the μ-3 sulfide S 1s → Fe 3d transitions, and the higher energy feature at ~2470.9 eV is due to the thiolate S 1s → Fe 3d transitions. Both gain intensity through S 3p mixing into Fe 3d orbitals. For both unbound and DNA bound EndoIII, lyophilization decrease the pre-edge intensity. Notably, redissolving lyophilized EndoIII results in XAS spectra indistinguishable from samples that were never dried, consistent with UV-visible and CD spectra and providing further confirmation that lyophilization does not dramatically alter the protein (Figure 3.1c). Likewise, for both solution and lyophilized data sets, DNA binding increases the pre-edge intensity, indicating that the Fe-S bonds become more covalent. DNA binding in solution increases the total S covalency from 573% to 631% (Table 3.1). On the basis of our past studies, each % increase of total S covalency corresponds to ~3.3 mV decrease in redox potential (*7*). Thus, the covalency increase upon DNA binding in Figure 3.1 and Table 3.1 corresponds to a decrease of the reduction potential of the $[4Fe4S]^{3+/2+}$ couple in EndoIII by ~190 mV, which would activate this cluster for oxidation. Critically, the DNA-induced potential shift measured by XAS is nearly identical to that measured electrochemically (*12*).

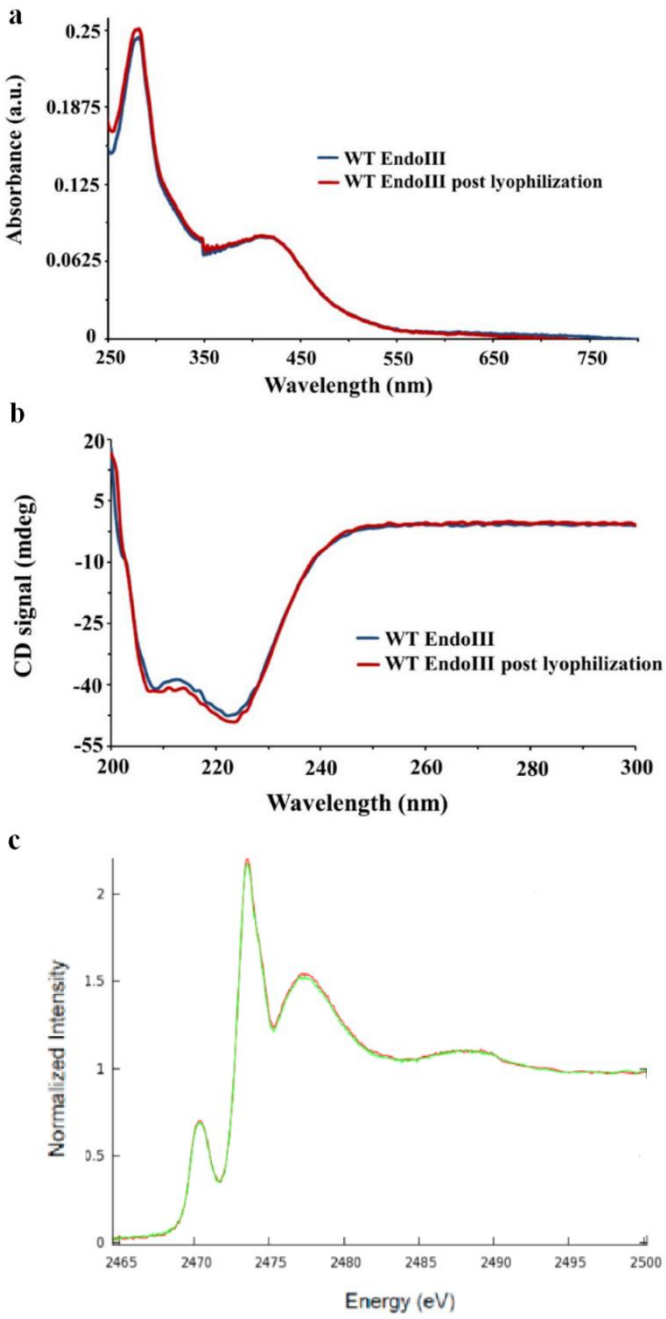

Figure 3.1 Spectroscopic data to confirm that lyophilization does not perturb the global structure of EndoIII or the cluster itself. UV-visible spectra (a) and circular dichroism (CD) spectra (b) taken with untreated sample and sample redissolved post-lyophilization are indistinguishable, confirming that cluster loading and local environment, as well as global protein folding, are unaltered by lyophilization. Consistent with this data, S K-edge XAS spectra taken of solvated EndoIII and a redissolved sample that had been previously lyophilized overlay almost perfectly (c).

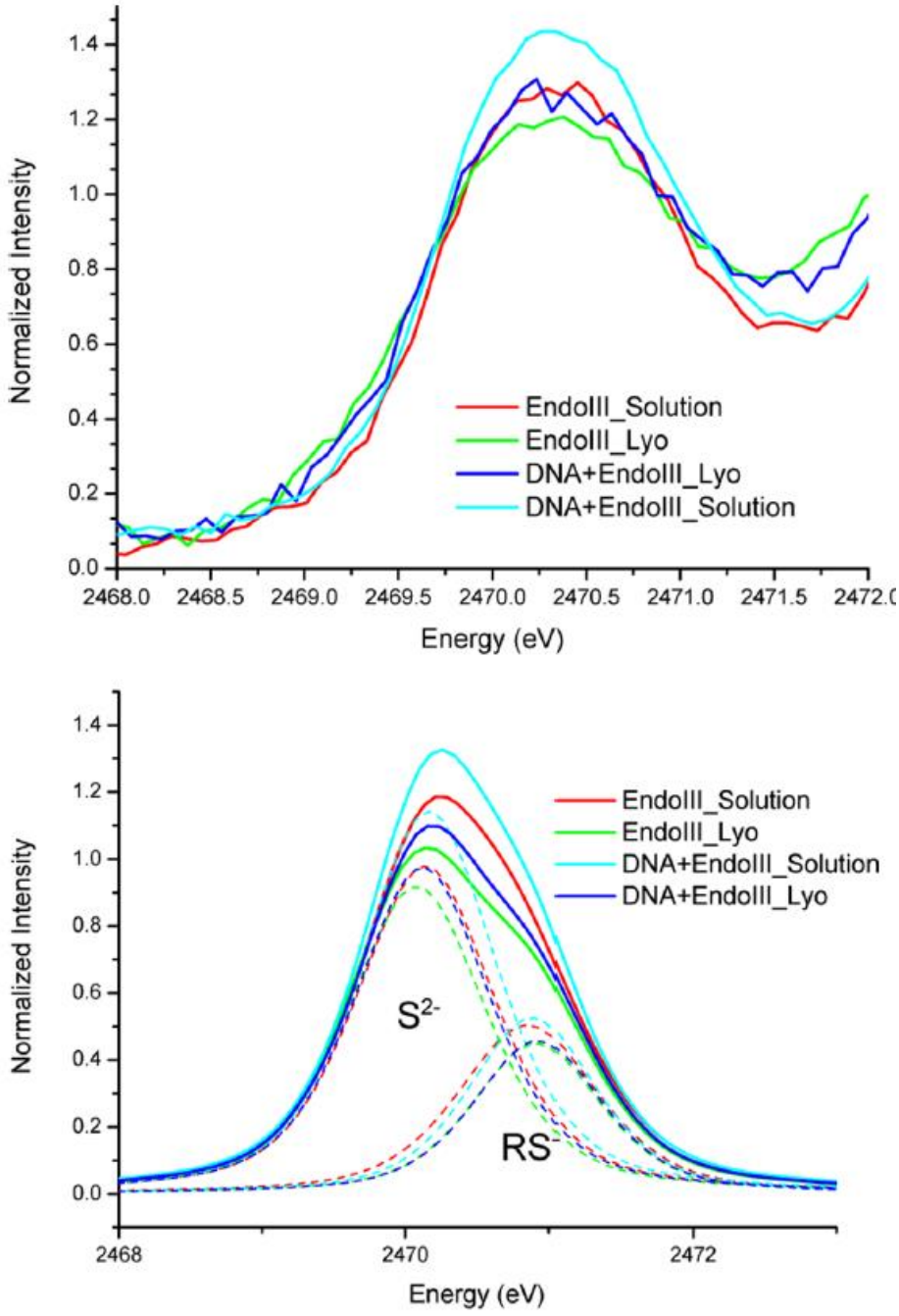

Figure 3.2 S K-edge XAS of EndoIII without and with DNA and upon lyophilization (top) and the fits of the pre-edge region (bottom) using two peaks, one for the sulfides at ~2470.1 eV and one for the thiolates at ~2470.9 eV.

Table 3.1 S K-edge XAS Data for $[4Fe4S]^{2+}$ Models and Proteins

Sample name		Energy (eV)	Area	Covalency (% per S)	Total Covalency
$[Fe_4S_4(SEt)_4]^{2-}$ model	Sulfide	2470.1	1.433	43.8	689.9±30
	Thiolate	2470.9	0.578	41.0	
Fd Solution	Sulfide	2470.1	1.145	35.0	555±23
	Thiolate	2470.9	0.481	34.0	
Fd Lyophilized	Sulfide	2470.1	1.276	39.0	620±27
	Thiolate	2470.9	0.523	37.0	
HiPIP Solution	Sulfide	2470.1	1.253	38.3	618.0±17
	Thiolate	2470.9	0.558	39.5	
HiPIP Lyophilized	Sulfide	2470.1	1.194	36.5	588.4±15
	Thiolate	2470.9	0.503	35.6	
EndoIII Solution	Sulfide	2470.2	1.185	36.2	572.8±28
	Thiolate	2470.9	0.488	34.5	
EndoIII Lyophilized	Sulfide	2470.1	1.056	32.3	522.6±25
	Thiolate	2470.9	0.477	33.8	
EndoIII+DNA Solution	Sulfide	2470.2	1.293	39.5	631.2±30
	Thiolate	2470.9	0.553	39.2	
EndoIII+DNA Lyophilized	Sulfide	2470.1	1.106	33.8	542.2±26
	Thiolate	2470.9	0.482	34.1	

S K-edge XAS of MutY in the Absence and Presence of DNA

S K-edge XAS of MutY without and with DNA are shown in Figure 3.2. Data were treated just as with EndoIII, except that MutY spectra required correction for eighteen rather than six nonbonding sulfur atoms. As with EndoIII, controls were performed to ensure that lyophilization pretreatment did not affect the protein. For MutY, these controls consisted of active site titrations using a ^{32}P-labeled 30-mer duplex containing a central oxoG:A mispair (Figure 3.3) (*26*). Under conditions of rate-limiting product release (burst kinetics), burst amplitudes, which correlate to active site concentration, exhibited no significant differences between samples.

XAS spectra reveal that, similar to EndoIII, the pre-edge intensity increases upon DNA binding, and decreases upon lyophilization (Figure 3.4). This is consistent with the fact that the N-terminal domain of MutY is structurally similar to EndoIIII in the presence of DNA (Figure 3.5). Notably, while MutY and EndoIII are structurally homologous, MutY shows specificity for adenine mispaired with 8-oxoguanine, whereas EndoIII targets a range of oxidized substrates. Incorporating 2′-deoxy-2′-fluoroadenosine (FA) in place of A across from an oxoG site generates a non-hydrolysable substrate mimic that enhances DNA binding affinity in MutY (*27*). Thus, to assess differences in non-specific and target DNA binding in MutY, the S K-edge XAS were measured both in the presence of specific (oxoG:FA) and non-specific DNA and with different DNA pair lengths under the same conditions as for EndoIII. One difference between MutY and Endo III is that MutY has an extra domain (Figure 3.5) that plays an important role in OG recognition and proper engagement of MutY on the oxoG:A substrate mispair (*28*). Figure 3.4

shows that in the case of MutY only the presence of specific DNA leads to the pre-edge intensity increase, and that the length of the DNA strand (15 and 30 base pairs) does not impact these intensity changes. This may be a consequence of affinity and MutY conformation with specific versus nonspecific DNA. MutY has much higher affinity for substrate-like DNA over nonspecific DNA, and MutY also induces dramatic remodeling of its substrate. However, there are more non-bound sulfur atoms in MutY than in EndoIII contributing to the background and precluding quantification of the changes in Figure 3.4.

Figure 3.5a shows that MutY and EndoIII not only are similar in conformation but share a set of conserved Arg residues that are responsible for DNA binding. Figure 3.5b and c show that these Arg locations are not perturbed by the DNA in EndoIII, although these two structures (both for *E. coli* protein homologues) share only 43% sequence similarity.

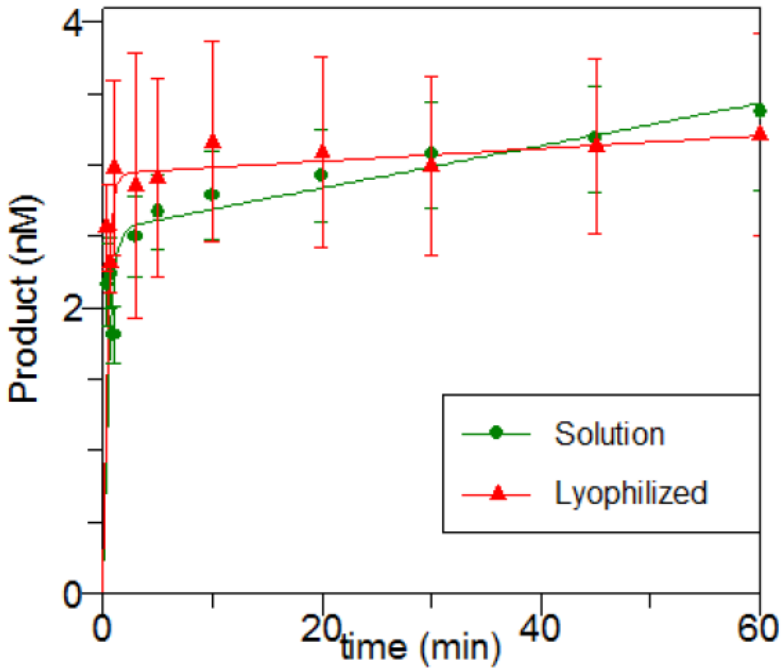

Figure 3.3 Average product curves and standard error bars of three separate aliquots each of solution (green) and lyophilized (red) MBP-MutY to determine the percent active fraction under maximum turnover conditions.

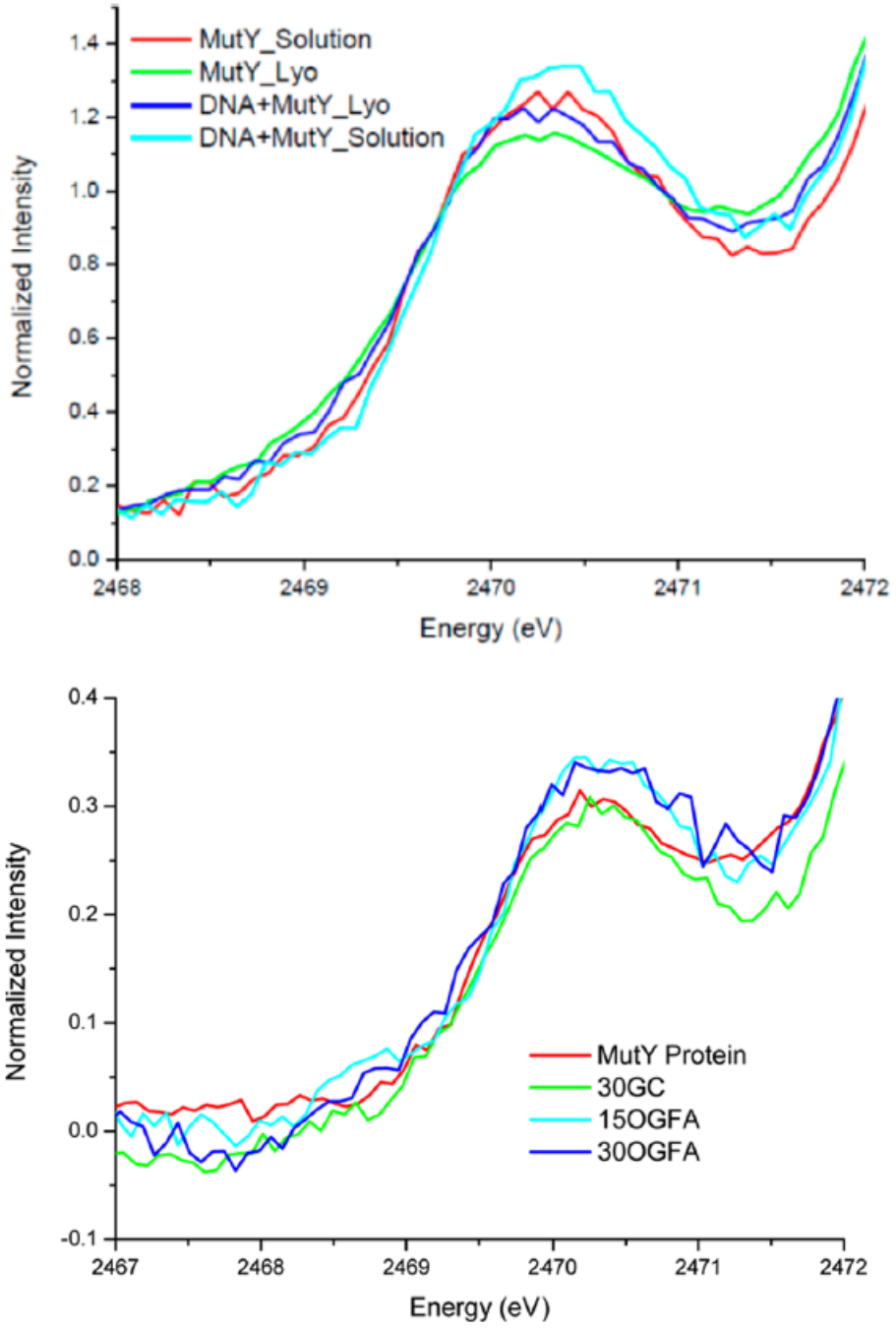

Figure 3.4 S K-edge XAS of MutY without and with nonspecific DNA and upon lyophilization (top), and S-K edge spectra showing impact of different DNA length (15 or 30) and of specific (OG:FA) as well as non-specific (GC) binding on MutY (bottom).

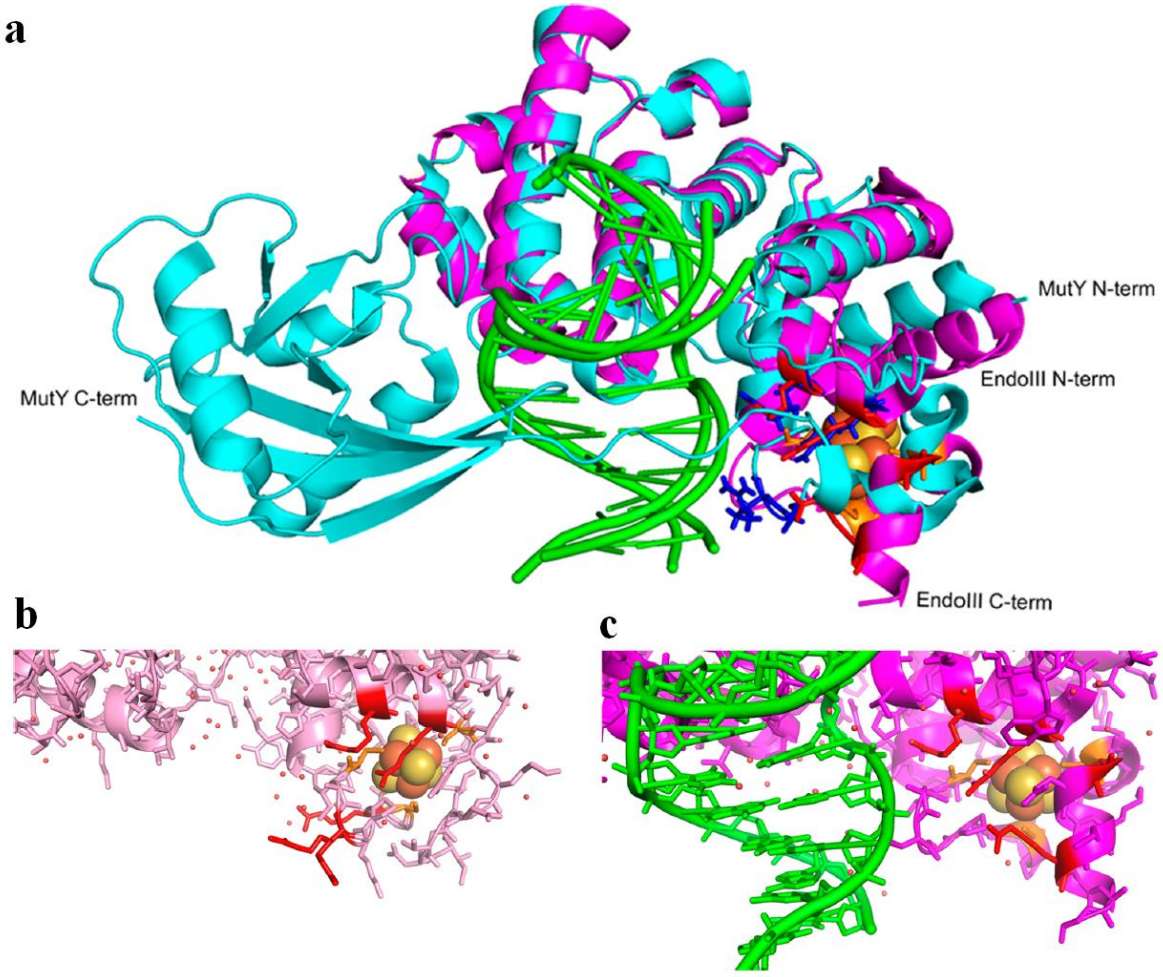

Figure 3.5 (**a**) Overlay of *G. stearothermophilus* (*Gs*) EndoIII (magenta, PDB 1ORN) and *Gs* MutY (cyan, PDB 5DPK), with [4Fe4S] cluster (orange for S and yellow for Fe atoms) and key Arg residues highlighted (red and blue, respectively). Bound DNA in both structures is green. (**b**, **c**) Comparison of *Ec* EndoIII without DNA (pink, PDB 2ABK) in (**b**) and *Gs* EndoIII (magenta, PDB 1ORN) bound to DNA (green) in (**c**) showing the molecular surroundings of the [4Fe4S] cluster, including critical Arg residues (red). This comparison highlights the overall structural similarity between *Gs* EndoIII in complex with DNA to that of the *Ec* homologue without DNA. Small structural differences ($RMSD_{100}$ = 1.4 Å) between the two homologues are attributed to their 43% sequence similarity.

Solvent Effect on HiPIP-Type Proteins

From our previous studies, lyophilization perturbs the H-bond environment around the [4Fe4S] cluster sites. For the studies described below, the spectroscopic features and protein activity were measured upon redissolving the lyophilized proteins to make sure that the lyophilization process did not lead to irreversible denaturation. Figure 3.2 and Table 3.1 show that upon lyophilization, the sulfur covalency of EndoIII decreases by ~50% total sulfur character out of ~570%, which is opposite to the solvent effect observed for [4Fe4S] *Bacillus thermoproteolyticus* ferredoxins (*Bt* Fd) (*7*). The pre-edge intensity of the [4Fe4S] cluster in *Bt* Fd increases by ~65% total sulfur character out of ~555% upon removal of solvent water. Unlike *Bt* Fd, where the [4Fe4S] cluster is exposed at the surface, EndoIII has a buried [4Fe4S] cluster, similar to MutY and *Chromatium vinosum* HiPIP. The XAS spectra of EndoIII (Figure 3.2), MutY (Figure 3.4) and *C. vinosum* HiPIP (Figure 3.6) all show a decrease in S pre-edge intensity with lyophilization (~30% out of a total of 618% sulfur character for HiPIP).

As shown in Figure 3.7a, the [4Fe4S] cluster in HiPIP (PDB code 1CKU) has five H-bonds from the protein environment to the thiolate sulfurs within 3.5 Å, all from the amide backbone. The higher S K-edge intensity in HiPIP relative to Fd and its decrease in S covalency upon lyophilization indicate that, relative to [4Fe4S] Fd, the H-bonds to [4Fe4S] cluster in HiPIP are weak. Removal of the solvent in HiPIP would lead to a more compact site, increasing the backbone H-bonds to the cluster. Also, three of the amides are solvent exposed, which could be directly affected by lyophilization (boxed). Furthermore, there are waters H-bonded to the

carbonyls that are conjugated to the amide N atoms, and removal of these water would enhance their N-H...S hydrogen bonds.

Figure 3.7b shows that in the DNA-free form of EndoIII (PDB code 4UNF), the [4Fe4S] cluster has six H-bonds to thiolate sulfurs within 3.5 Å: one from arginine, one from histidine, and four from the amide backbone. Figure 3.7c shows a similar H-bond pattern around the cluster for DNA-bound EndoIII (PDB code 1ORN). In EndoIII, the increased number of H-bonds and the stronger H-bond from the positively charged Arg are consistent with the somewhat lower S covalency of EndoIII relative to that of HiPIP (Table 3.1, solution: 573% vs 618%; lyophilized: 523% vs 588% for EndoIII and HiPIP, respectively). In addition to the more compact site that would result from lyophilization, the Arg, His, and amides are all at the surface of the protein and would also be directly impacted by loss of H_2O (red dots in Figure 3.5 and boxed region in Figure 3.7b and c). The larger number of surface exposed H-bonds is consistent with the larger decrease in S edge intensity in EndoIII relative to HiPIP upon lyophilization (50% vs 30% respectively). MutY has a similar DNA binding domain structure to EndoIII, and a surface Arg is shown in blue in Figure 3.5a.

Finally, as displayed in Figure 3.2 and Table 3.1, lyophilization of DNA bound EndoIII also leads to an intensity decrease (somewhat larger than for the unbound EndoIII). Thus even when bound to DNA, there is solvent access to the [4Fe4S] cluster in EndoIII.

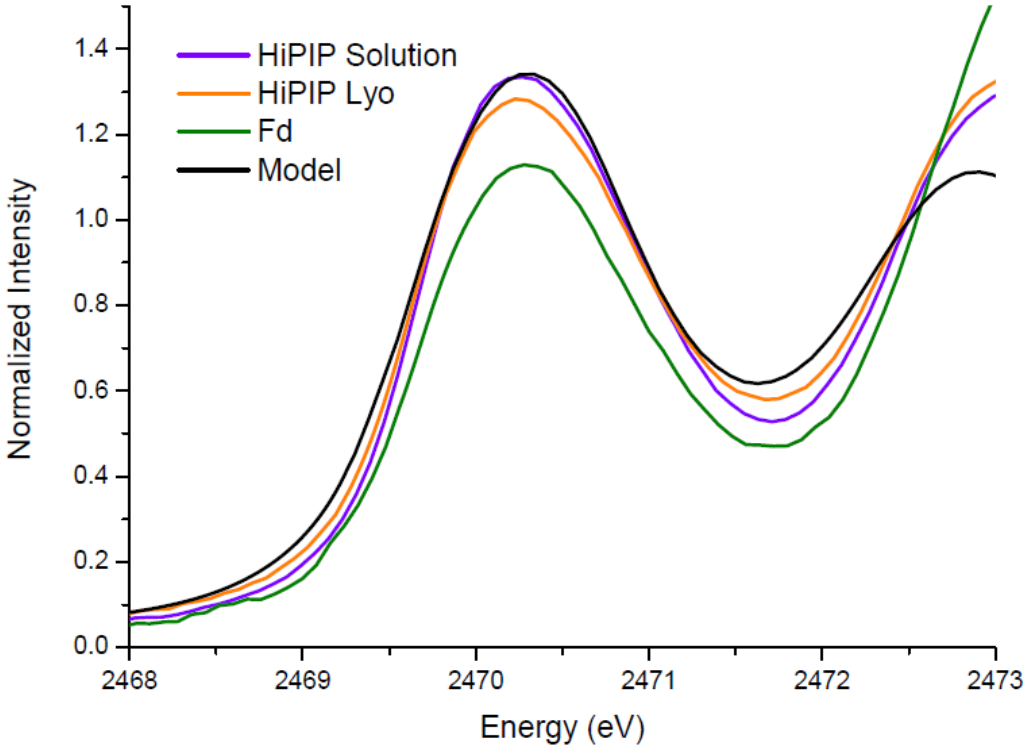

Figure 3.6 S K-edge XAS spectra of HiPIP compared with a model and Fd. As with EndoIII, HiPIP pre-edge absorbance is highest for solvated sample. In all cases, however, HiPIP absorbance is much higher than that of Fd, consistent with lower solvent exposure of the cluster in HiPIP.

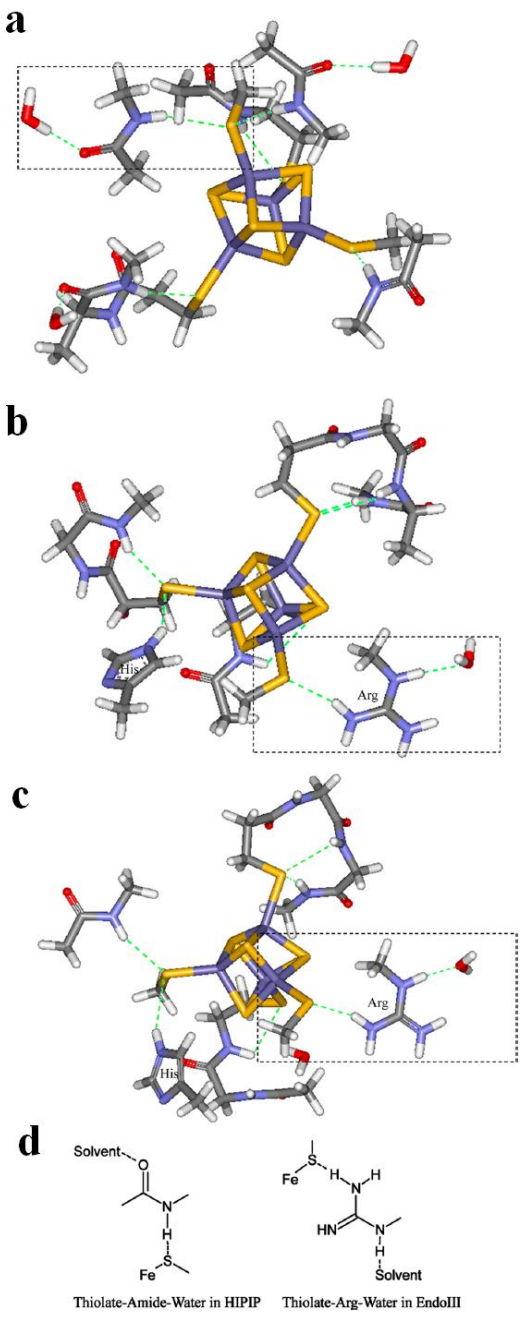

Figure 3.7 Local H-bond network of the Fe_4S_4 cluster for (**a**) HiPIP (PDB code 1CKU) and (**b**) EndoIII without DNA (PDB 4UNF) and (**c**) with DNA (PDB 1ORN), illustrating some of the H-bonds that could be affected by solvent water. The H-bonds are shown in dashed green, and Arg and His are labeled. Schemes of the boxed region are shown in (**d**). In (**a**), an amide backbone H-bond to the thiolate S bound to Fe and accessible solvent is shown in the box, and in (**b**) and (**c**), an arginine residue H- bond to the thiolate bound to Fe and accessible to solvent is shown in the box.

DFT Calculations

DNA is rich in negative charge. To qualitatively test whether the presence of negative charge would increase total [4Fe4S] sulfur covalency and understand the nature of this effect, simple models were evaluated. The results are shown in Table 3.2.

Placing a negative point charge 5 Å away from one thiolate increases the total sulfide and thiolate contributions from 429.0% to 439.1% and from 139.3% to 144.8% respectively, which correspond to a total sulfur contribution increase from 568.4% to 583.9%. This is qualitatively similar to experiment but the effect is less than observed experimentally due to the simple model. Placing a negative point charge 5 Å from one sulfide gave similar results (Table 3.2); the total sulfide and thiolate contributions increased to 438.3% and 143.9% respectively, and total sulfur contribution increased to 582.2%.

The DFT calculations in Table 3.2 show that the addition of the negative charge near the [4Fe4S] cluster can qualitatively model the increase in covalency observed with DNA binding and thus provide insight into the origin of this effect. Figure 3.8 gives the change in Mulliken charge distribution (a), Mayer bond orders (MBO) (b) and C^2 contributions (c, which sums the contributions of the valence atomic orbitals over the unoccupied valence molecular orbitals, for each Fe and S atom of the cluster) due to the addition of the negative point charge. The change in C^2 would directly relate to the change in S edge intensity observed experimentally. The changes calculated for placing the point charge next to a thiolate are given in blue, and next to a sulfide are given in red.

Adding a point charge near the thiolate (Figure 3.8, blue) results in a shift of the electron density toward the opposite side of the cluster (a). The thiolate next to the point charge (denoted S*) loses electron density (change in Mulliken charge +0.13), while the three thiolates and one sulfide on the opposite side of the cluster gain some negative charge (~ -0.03, A). Thus S* donates more charge density to the Fe it coordinates (denoted Fe*); this is reflected in its increase in MBO (+0.12 for Fe*-S* in B). The three sulfides that coordinate to Fe* then donate less to it to compensate (MBO ~-0.01 each in b), but donate more to the remaining Fe's (MBO ~+0.01). The other three thiolates have decreased MBO (-0.02 each in b) as they now donate less charge density to their coordinated Fe atoms, which is consistent with their increase in negative Mulliken charge (a). Although there are some compensation effects, the total MBO increases (+0.06). In terms of C^2 (Figure 3.8c), because the Fe*-S* bond becomes stronger (from the MBO), more S 3p character is mixed into the unoccupied Fe 3d orbitals, leading to the increase in S* C^2 contribution (+3.4) and decrease of the Fe* contribution (-4.9). Although the other three sulfide bonds to Fe* get slightly weaker (from the MBO in b), these sulfides have net higher C^2 (+4.6, -0.4, +3.4 in C). The negative point charge at S* destabilizes the occupied S p orbital energies (Scheme 1), which results in more S character mixed into the unoccupied valence molecular orbitals. The Fe d characters all decrease in response to the increase of S p, and both sulfide and thiolate C^2 increase as observed experimentally.

Similar effects were observed when placing the point charge 5Å away from the sulfide at the corner of the cube (Figure 3.8, red). Note that except for the S atom and Fe-S bond(s) closest to

the charge, there is only a limited change in Mulliken charge, MBO and C^2 contributions for the rest of the cluster. The net change is an increase in C^2 character, again qualitatively consistent with the S K-edge XAS experimental data.

Table 3.2 Results of DFT Calculation

Model	Total Fe %	Total Sulfide %	Total Thiolate %	Total S %
$[Fe_4S_4(SMe)_4]^{2-}$ model	958.4	429.0	139.3	568.4
$[Fe_4S_4(SMe)_4]^{2-}$ with $1e^-$ at 5Å from sulfide	944.1	438.3	143. 9	582.2
$[Fe_4S_4(SMe)_4]^{2-}$ with $1e^-$ at 5Å from thiolate	949.3	439.1	144.8	583.9

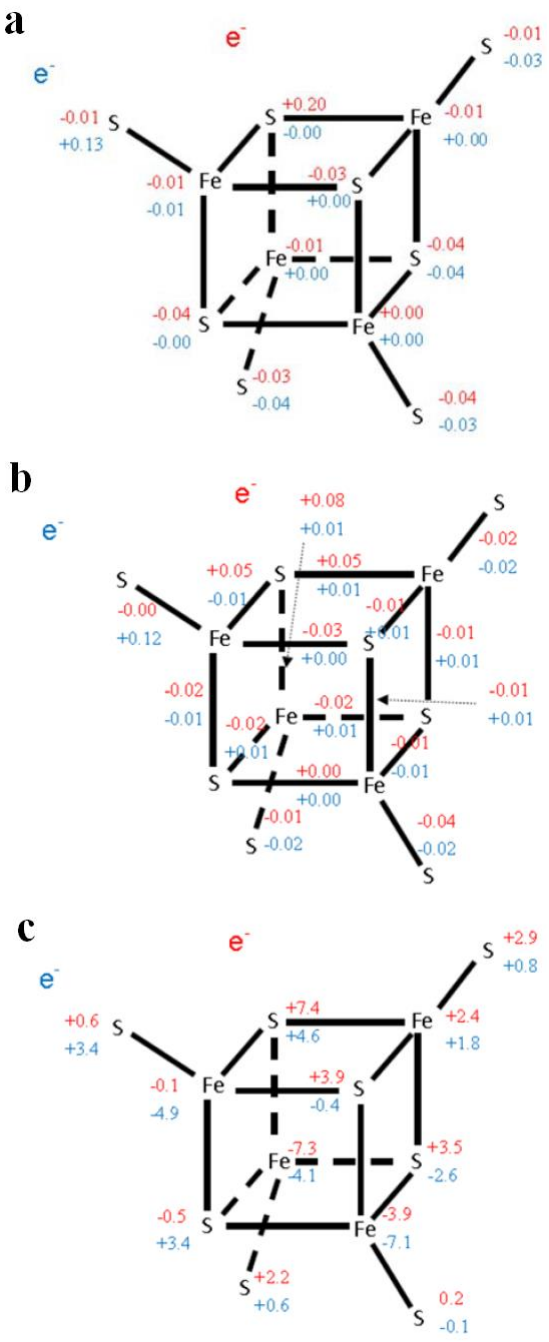

Figure 3.8 Difference in Mulliken charge distribution (**a**), Mayer bond orders (MBP) (**b**) and C2 contributions (**c**) of each Fe and S atom of the cluster without and with a point charge at 5 Å distance from the cluster. Blue represents values obtained for a point charge near a thiolate S, and red represents those for a point charge near a sulfide S.

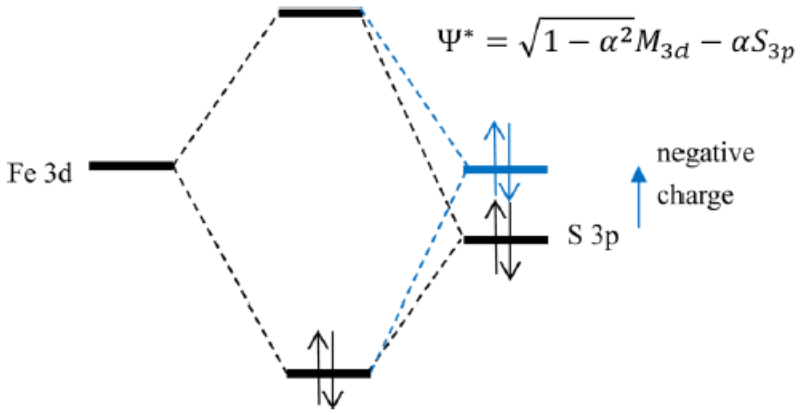

Scheme 3.1 Adding negative charges such as DNA in the proximity of the [4Fe4S] cluster destabilizes the S 3p orbital energy and increases the S 3p character (α^2) in Ψ*. This increases the Fe-S covalency and stabilizes the oxidized form than the reduced form of the cluster and decreases the reduction potential.

Spectroscopic Characterization of EndoIII Point Mutants

To see if shifting the charges near the [4Fe4S] cluster in EndoIII might alter the redox potential, we prepared a series of point mutants (E200K, Y205H, and K208E) in which the altered residues are all within 5 Å of the cluster (*19*). By changing a single charge from negative to positive (E200K) or vice versa (Y205H, K208E), we reasoned that it might be possible to shift the redox potential both negative, like DNA, and in the opposite direction. However, no evidence for a shift was seen in these mutants when bound to DNA on a gold electrode, nor was a difference observed by direct electrochemistry of DNA-free protein on edge plane graphite (*19*, *29*). The error in the latter experiments, however, did not preclude a small shift on the order of 10 mV. Overall, we wished to use S K-edge XAS as an independent means of assessing the potential in these mutants.

Solvated and lyophilized samples of each mutant were prepared in the absence and presence of DNA exactly as with WT EndoIII, and spectra were taken alongside a WT sample. Consistent with previous electrochemical results that show no potential shift in these mutants, the pre-edge absorbance of E200K overlay WT EndoIII almost perfectly; results with DNA present are inconclusive due to noise (Figure 3.9) (*7*). The pre-edge features of both Y205H and K208E are much lower than expected for HiPIP-type proteins; indeed, K208E is well in the range of Fd, and Y205H is lower still, suggesting a redox potential below -500 mV vs NHE (Figure 3.9). Such a large decrease in Fe-S covalency was wholly unexpected, and thus required further experimental follow-up. Other than a genuine potential shift in these mutants, possible

explanations included a different cluster absorbance at 410 nm (ε_{410}) than WT leading to inaccurate loading measurements and thus incorrect XAS corrections or cluster degradation before or during XAS measurements.

To address a possible difference in cluster absorbance at 410 nm, we used a combination of UV-visible spectroscopy, Bradford assays, and iron loading experiments to measure ε_{410} and [4Fe4S] loading in the same WT, Y205H, and K208E stocks used for XAS. In each case, total protein concentration and [4Fe4S] cluster absorbance were measured for three replicates each of WT EndoIII and each mutant, and an equal number of replicates were subjected to iron loading analysis to obtain total iron concentration in the sample. By this analysis, ε_{410} values were determined to be 17618 ± 229 $M^{-1}cm^{-1}$, 16661 ± 221 $M^{-1}cm^{-1}$, and 18008 ± 135 $M^{-1}cm^{-1}$ for WT, K208E, and Y205H, respectively. Notably, none of these differs appreciably from the assumed value of 17000 $M^{-1}cm^{-1}$, and cluster loading determined by Bradford assays using these updated values was not greatly altered, indicating that the unexpected XAS results did not occur as a miscalculation of cluster loading.

Having confirmed that cluster loading calculations could not have caused the discrepancies in pre-edge absorbance, we sought an independent technique to probe the cluster environment of the EndoIII mutants. Previous electrochemical results with DNA present suggested that the cluster environment of the mutants was dominated by DNA binding, in contrast to the XAS results. In an effort to resolve this issue, we compared UV-visible spectra of WT and mutant EndoIII in the presence and absence of DNA, reasoning that any changes in

cluster electronic environment induced upon DNA binding should be similar between all EndoIII variants if the differences seen by XAS were due to sample degradation. In three replicates of WT EndoIII, the broad absorbance of the [4Fe4S] cluster did not change markedly in the presence of DNA, although a slight increase in absorbance was consistently present (Figure 3.10). These data suggest that DNA binding does induce a very minor, but still detectable, change in cluster electronics that could be used to compare WT and mutants. These experiments were repeated with E200K, Y205H, and K208E, all of which showed a very similar small increase in absorbance upon DNA binding (Figure 3.10b). The similarity of absorbance changes in WT and all mutants confirms that DNA binding has the same effect on cluster electronics as WT, supporting previous electrochemical results and suggestive of sample degradation in the XAS experiments.

At this point, our experiments indicated that the iron loading in XAS samples was correct, and that neither Y205H nor K208E was noticeably different by UV-visible absorbance at 410 nm in the presence of DNA. Previous electrochemical, melting temperature, and CD analysis suggested that the cluster is more solvent-exposed in Y205H and K208E, lowering their stability relative to WT, while E200K is more shielded and of comparable or greater stability than WT (*19*). To see if low stability might explain the XAS results, we carried out X-band EPR spectroscopy at 10 K with WT, E200K, Y205H, K208E, and an additional mutant, Y82A (Figure 3.11). Y82A is known to be CT-deficient in the presence of DNA, but is expected to have an identical cluster environment to WT (*19*); thus, this mutant served as an additional control for

these experiments. To probe cluster stability, we treated protein samples in the absence of DAN with $K_3Fe(CN_6)$ in varied molar equivalents. $K_3Fe(CN)_6$ does not oxidize EndoIII very effectively in the absence of DNA, but a quantifiable signal centered at g = 2.02 attributable to a $[Fe_3S_4]^+$ cluster can nonetheless be observed at a sufficient excess of oxidant (*8, 11*). If some mutants were unstable, they would be expected to be more sensitive to such treatment than WT.

As expected, 20 μM WT EndoIII was EPR silent when untreated and showed a clear $[3Fe4S]^+$ signal at g = 2.03 when treated with a molar excess of oxidant (Figure 3.11a). Signal size increases linearly with increasing oxidant concentration, although some signal loss occurrs at 10-fold excess $K_3Fe(CN)_6$ when samples were not frozen immediately after treatment. The latter effect is consistent with oxidative degradation. To minimize this risk, EPR spectra of EndoIII mutants were initially taken at a 5-fold molar excess of $K_3Fe(CN)_6$. Like WT, all mutants are EPR silent when untreated. Y82A signals are as large or larger than those of WT, confirming that the cluster environment in this mutant is, as expected, unaltered. K208E spectra are slightly smaller than WT in the presence of 5-fold molar excess $K_3Fe(CN)_6$, while E200K and Y205 are both much smaller (Figure 3.11b). E200K signals could be increased by including a 10-fold excess of oxidant, but still remained much smaller than those of WT; these results are in agreement with previous work suggesting a more solvent-shielded cluster in this mutant. In contrast, Y205H signals decreased with 10-fold excess oxidant, and were much more sensitive to incubation time than any other EndoIII variant. To see if better signals could be obtained, we tried treating Y205H with 0.5, 1, and 3-fold excess oxidant; signals increased linearly up to 3-

fold excess, and were similar to those obtained at 5-fold excess. These data support the previously mentioned instability of Y205H; furthermore, UV-visible spectra of some (but not all) stocks sent for XAS showed increased absorbance associated with oxidative degradation after one additional freeze-thaw cycle. In summary, our EPR results are in agreement with previous studies, indicating greater instability in the Y205H cluster. EPR spectra did not show any significant differences between K208E and WT, but the bulk of previous evidence supports cluster instability in this mutant as well, although to a lesser degree than Y205H.

Overall, the XAS results for EndoIII mutants are equivocal. E200K spectra fit the expected pattern and match previous results, but K208E and, especially, Y205H appear to be too unstable to carry out reliable experiments. Thus, the unexpectedly low pre-edge absorbance seen in the Y205H and K208E XAS spectra most likely reflects cluster degradation rather than an actual shift to a Fd-like environment.

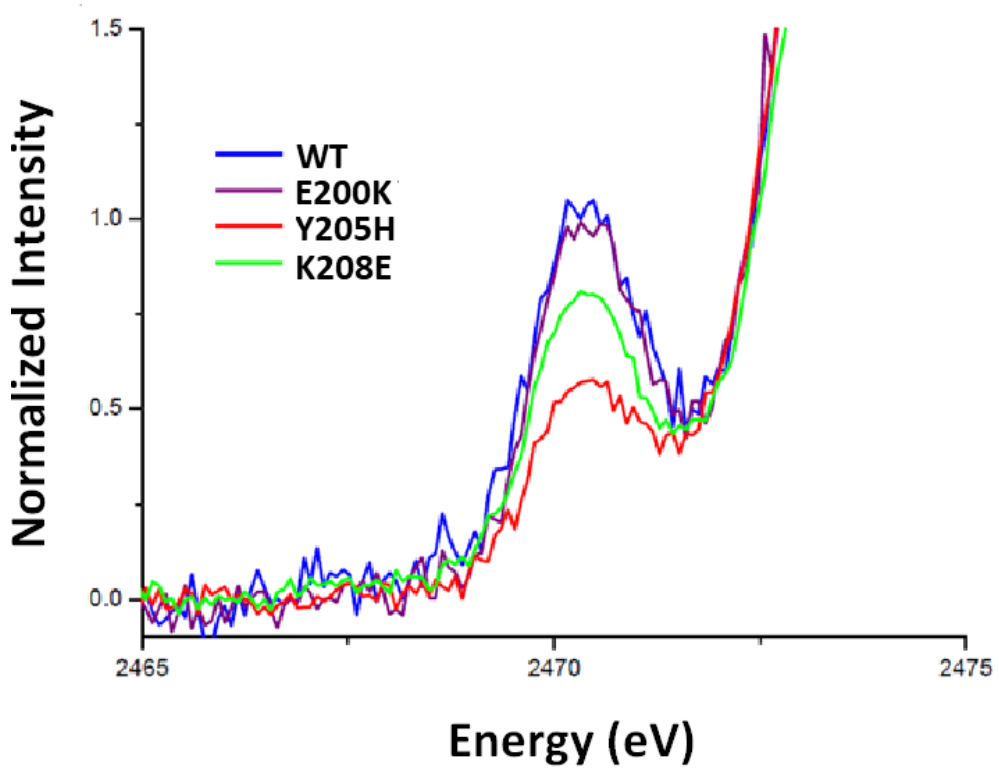

Figure 3.9 S K-edge XAS spectra of WT EndoIII and the mutants E200K, Y205H, and K208E. These mutations all reside within 5 Å of the cluster, and were intended to alter the local environment sufficiently to induce a shift in potential. E200K overlaid well with WT, consistent with electrochemical experiments, while K208E and Y205H showed pre-edge absorbance more similar to Fd than HiPIP or the other EndoIII variants. The latter results were likely due to cluster degradation in these less stable mutants.

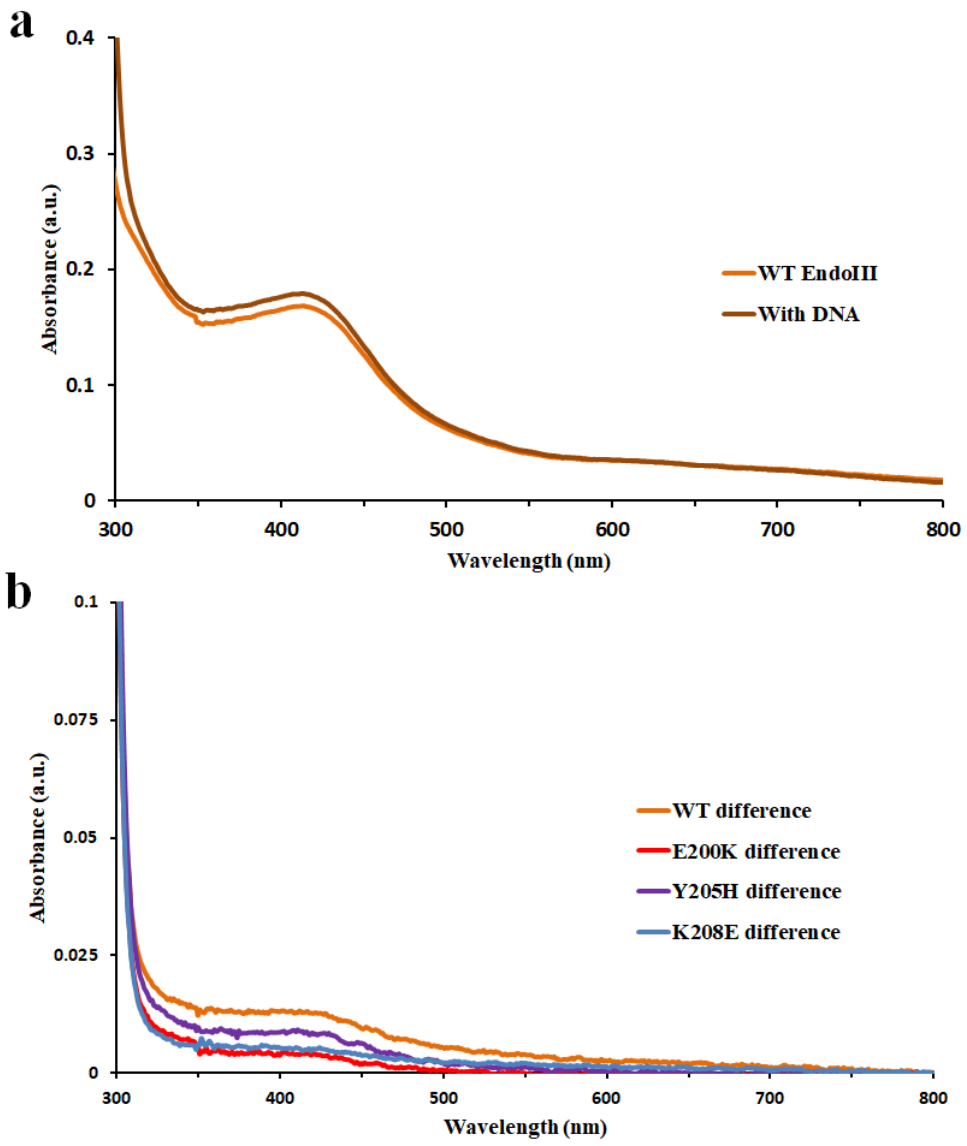

Figure 3.10 UV-visible spectra of WT EndoIII and the mutants E200K, Y205H, and K208E with and without DNA present. WT EndoIII shows very little difference in absorbance at these wavelengths (**a**), with only a slight increase most easily seen in subtraction spectra (**b**). The other mutants were similar, indicating no significant differences in cluster environment upon DNA binding.

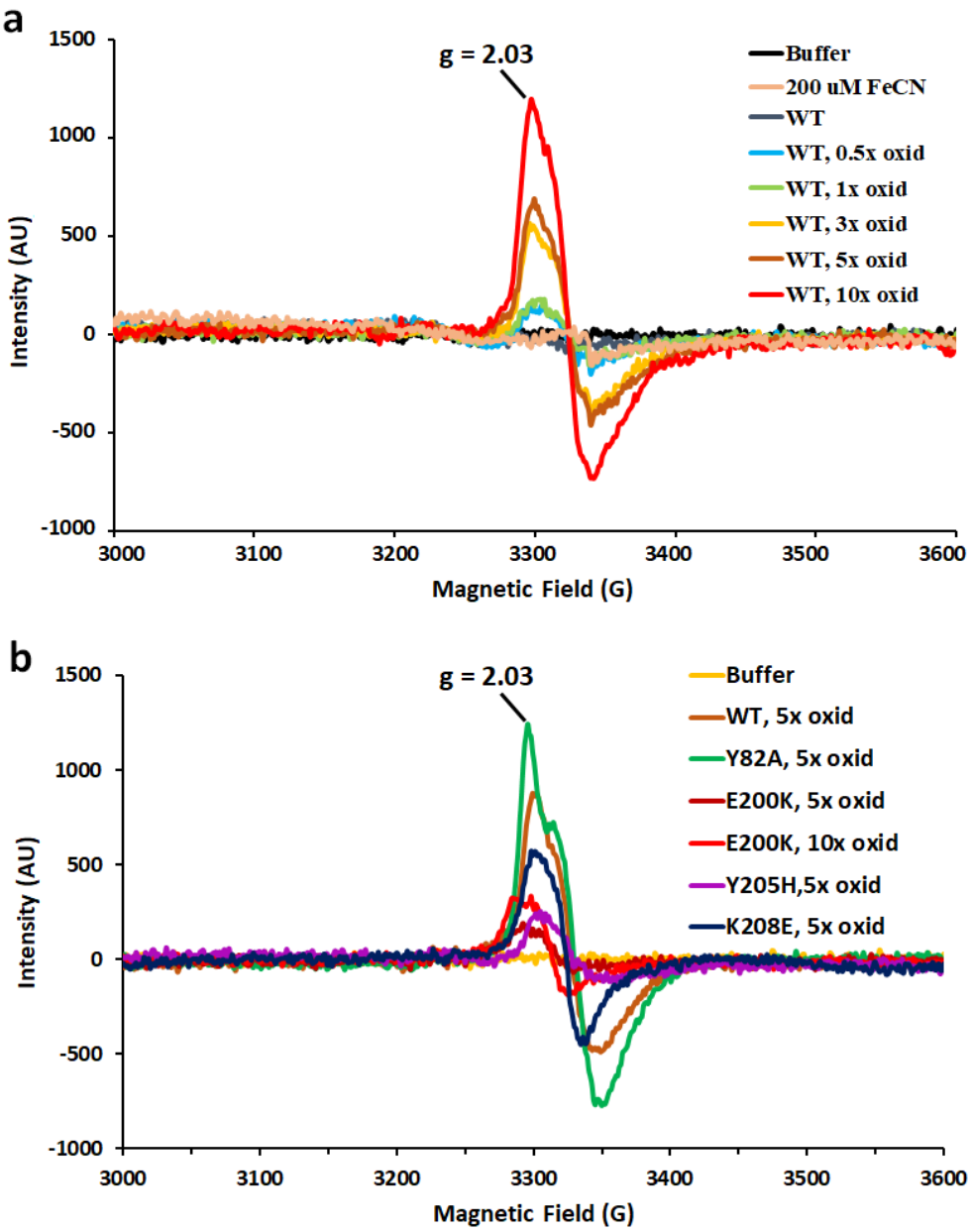

Figure 3.11 Continuous wave X-band EPR spectra of 20 μM WT EndoIII (**a**) and the mutants Y82A, E200K, Y205H, and K208E treated with $K_3Fe(CN_6)$ in the indicated molar excess (**b**). All variants are EPR silent when untreated and show formation of the $[3Fe4S]^+$ oxidative degradation product in the presence of $K_3Fe(CN)_6$. WT and Y82A yield substantial signals, while E200K is markedly less sensitive to oxidation. Y205H is highly susceptible to oxidation and degradation, giving the largest signals with 3-fold excess oxidant. K208E was similar to WT, although signals were slightly smaller. All spectra were taken at 10 K, 12.88 mW microwave power, 5.03 x 10^3 receiver gain, and are the average of 3 scans.

Discussion

Both EndoIII and MutY contain [4Fe4S] clusters that are largely redox inert in solution, but their reduction potentials decrease by ~200 mV upon DNA binding to turn on their function in DNA damage recognition. In nature, a large number of proteins also have [4Fe4S] clusters, with a wide range of reduction potentials (Fd: -700 to -300 mV; HiPIP: 100 to 400 mV) (*1*) (Scheme 2). S K-edge XAS has been found to be a powerful technique to evaluate the contributions of H-bonds and electrostatics to the reduction potentials of these [4Fe4S] clusters (*30*). From our past studies on Fd and HiPIP, the redox properties of these [4Fe4S] clusters are highly related to their local protein environment (*7*). In Fd, the [4Fe4S] cluster is at the surface of the protein. There are strong H-bonds from solvent water, and the Fe-S bonds are less covalent. This raises the reduction potential of the +2 state and results in the $[4Fe4S]^{2+/1+}$ redox couple in the physiological potential range. Upon lyophilization, the S covalency significantly increases due to the loss of H-bonds from solvent to the [4Fe4S] cluster and the covalency becomes similar to that of HiPIP. In contrast, HiPIP, which is not solvent exposed, has only weak H-bonds from the backbone amides to the iron-sulfur cluster, and thus more covalent Fe-S bonds. In HiPIP, the $[4Fe4S]^{3+/2+}$ redox couple is activated in the physiological potential range (Scheme 2). In the present study, lyophilization of HiPIP leads to an inverse effect on the Fe-S bond covalency relative to Fd (i.e. the covalency decreases). Loss of solvent would lead to a more compact site and increase the H-bonding to the [4Fe4S] cluster from backbone. Loss of water H-bonds to the

surface amides would further strengthen these H-bonds to the thiolates. Lyophilization results in a similar effect on EndoIII and MutY.

EndoIII and MutY both have a strong Arg H-bond to their $[4Fe4S]^{2+}$ cluster, which is consistent with the lower covalency relative to HiPIP and making the [4Fe4S]3+/2+ couple less accessible (Table 3.1). Overall, this behavior correlates with their lack of redox activity in the absence of DNA (*31, 32*). S K-edge XAS experiments show that DNA binding to EndoIII and MutY significantly increases their Fe-S bond covalency, while in EndoIII DNA binding lowers its $[Fe_4S_4]^{3+/2+}$ potential by ~200 mV into the physiologically accessible range. An alignment of the unbound and DNA bound structures of EndoIII (Figure 3.12) shows no significant distortion of the protein ($RMSD_{100}$ = 1.4 Å; note that these EndoIII proteins are homologues with 43% sequence similarity); thus, DNA binding does not appear to structurally affect its $[Fe_4S_4]$ site. DNA binding, although at a distance of ~15 Å from the [4Fe4S] cluster, does introduce significant negative charge into the system. For the iron-sulfur cluster, the negative charge would destabilize the occupied S p orbital energies, and result in more S character donated into the unoccupied valence Fe 3d-based molecular orbitals (Scheme 2). This increases the Fe-S bond covalency of the cluster, stabilizing the oxidized over the reduced state, and thus decreasing the reduction potential. Simple DFT models using a negative point charge to represent the effect of the DNA qualitatively reproduce this covalency increase and show that it dominantly involves an increase in electron donation from the S oriented toward the negative charge with some limited compensation by the remote sulfurs.

S K-edge XAS studies on iron sulfur proteins both alone and bound to DNA, and with and without solvent water show that the local environments of the [4Fe4S] clusters affect the covalencies of their Fe-S bonds and thus tune the potentials of the clusters. In Fd, the strong H-bonds from solvent reduces the covalency and stabilizes the reduced form of the cluster, while in HiPIP, the cluster is buried and with only weak amide H-bonds, stabilizing the oxidized form. In EndoIII and MutY the cluster is also buried but with an additional Arg H-bond that reduces the covalency relative to HiPIP and makes the HiPIP couple less accessible. However, binding to DNA introduces negative charge that increases the [4Fe4S] covalency for both EndoIII and MutY. Previous correlations between [4Fe4S] covalency and redox potential indicate that this decrease~~s~~ corresponds to an approximately 200 mV negative shift in reduction potential and would enable the $[4Fe4S]^{2+/3+}$ redox couple that is observed experimentally. Overall, the results obtained by XAS are in remarkably close agreement with electrochemical studies carried out with EndoIII in the presence and absence of DNA, indicating that the physical mechanism of the potential shift is a charge-induced increase in thiolate-iron bond covalency within the [4Fe4S] cluster. It is these molecular-level changes that are responsible for the remarkable ability of otherwise redox-inert repair proteins to communicate with each other over vast distances using reversible DNA-mediated charge transfer, making the daunting task of searching an entire genome for damage possible on a physiologically relevant time scale.

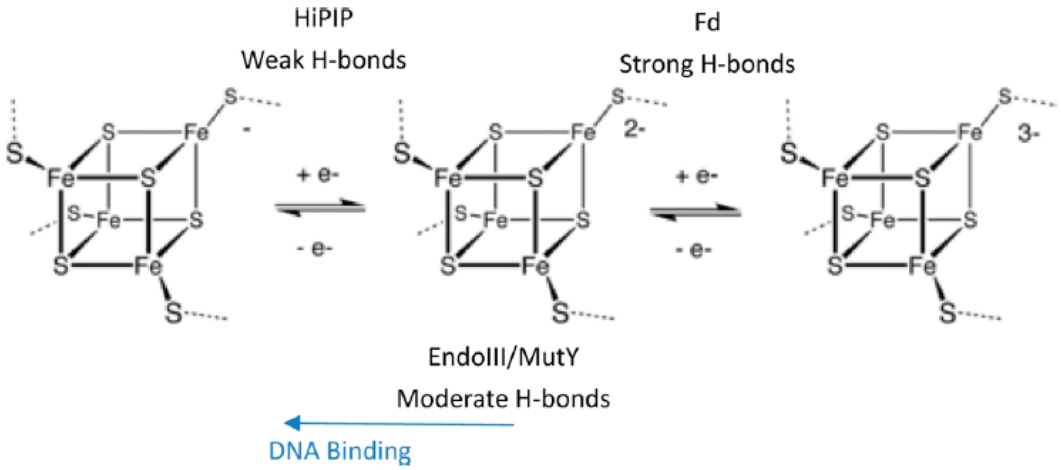

Scheme 3.2 Protein environment of the [4Fe4S] cluster tunes its redox couple. Fds have strong H-bonds to S (5 amide-thiolate H-bonds, 3 amide-sulfide bonds, and, more importantly, H-bonds to surface-exposed thiolate from solvent water) and thus the S donate less electron density to Fe, stabilizing the reduced state (redox potential range -300 to -700 mV). HiPIPs have only weak H-bonds to S (5 amide-thiolate H-bonds), thus these S donate more electron density to Fe, stabilizing the oxidized state (redox potential range 100 to 400 mV). EndoIII/MutY have moderate H-bonding (a few amide-thiolate H-bonds, and an Arg-thiolate H-bond), thus are largely redox inert. However, binding to DNA introduces negative charge, thus stabilizing the oxidized state and facilitating redox activity at potentials of ~80 mV vs NHE.

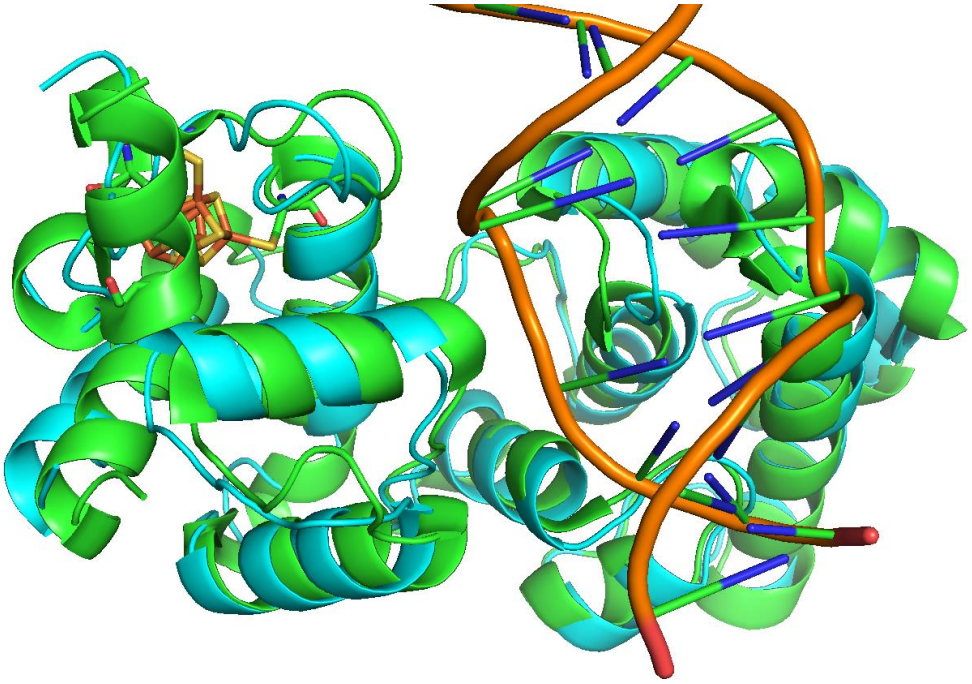

Figure 3.12 Structural alignment comparison of free (blue, PDB code 2ABK) and DNA bound (green, PDB code 1ORN) forms of EndoIII.

References

1) Holm, R. H.; Kennepohl, P.; Solomon, E. I. Structural and Functional Aspects of Metal Sites in Biology. *Chem. Rev.* **1996,** *96*, 2239 – 2314.

2) Stiefel, E. I.; George, G. N. Ferredoxins, Hydrogenases, and Nitrogenases: Metal-Sulfide Proteins. In *Bioinorganic Chemistry*, Bertini, I., Ed. University Science Books: Mill Valley, **1994**; pp 365 – 453.

3) Backes, G.; Mino, Y.; Loehr, T. M.; Meyer, T. E.; Cusanovich, M. A.; Sweeney, W. V.; Adman, E. T.; Sanders-Loehr, J. The environment of Fe4S4 clusters in ferredoxins and high-potential iron proteins. New information from x-ray crystallography and resonance Raman spectroscopy. *J. Am. Chem. Soc.* **1991,** *113*, 2055 – 2064.

4) Teo, B.-K.; Shulman, R. G.; Brown, G. S.; Meixner, A. E. EXAFS Studies of Proteins and Model Compounds Containing Dimeric and Tetrameric Iron-Sulfur Clusters *J. Am. Chem. Soc.* **1979,** *101*, 5624.

5) Czernuszewicz, R. S.; Macor, K. A.; Johnson, M. K.; Gewirth, A.; Spiro, T. G. Vibrational mode structure and symmetry in proteins and analogs containing Fe4S4 clusters: resonance Raman evidence that HiPIP is tetrahedral while ferredoxin undergoes a D2d distortion. *J. Am. Chem. Soc.* **1987,** *109*, 7178 – 7187.

6) Dey, A.; Glaser, T.; Couture, M. M.-J.; Eltis, L. D.; Holm, R. H.; Hedman, B.; Hodgson, K. O.; Solomon, E. I. Ligand K-Edge X-ray Absorption Spectroscopy of $[Fe_4S_4]^{1+,2+,3+}$ Clusters: Changes in Bonding and Electronic Relaxation upon Redox. *J. Am. Chem. Soc.* **2004,** *126*, 8320 – 8328.

7) Dey, A.; .JenneyJr, F. E.; Adams, M. W. W.; Babini, E.; Takahashi, Y.; Fukuyama, K.; Hodgson, K. O.; Hedman, B.; Solomon, E. I. Solvent Tuning of Electrochemical Potentials in the Active Sites of HiPIP Versus Ferredoxin *Science* **2007,** *318*, 1464 – 1468.

8) Boal, A. K.; Yavin, E.; Lukianova, O. A.; O'Shea, V. L.; David, S. S.; Barton, J. K. DNA-Bound Redox Activity of DNA Repair Glycosylases Containing [4Fe-4S] Clusters. *Biochemistry*. **2005,** *44*, 8397 – 8407.

9) Lukianova, O. A.; David, S. S. A role for iron–sulfur clusters in DNA repair. *Curr. Op. Chem. Biol.* **2005,** *9*, 145 – 151.

10) Manlove, A. H.; Nuñez, N. N.; David, S. S. The GO Repair Pathway: OGG1 and MUTYH. In *The Base Excision Repair Pathway*, III, D. M. W., Ed. World Scientific: **2016**; pp 63 – 115.

11) Cunningham, R. P.; Asahara, H.; Bank, J. F.; Scholes, C. P.; Salerno, J. C.; Surerus, K.; Munck, E.; McCracken, J.; Peisach, J.; Emptage, M. H. Endonuclease III is an iron-sulfur protein. *Biochemistry* **1989,** *28*, 4450 – 4455.

12) Gorodetsky, A. A.; Boal, A. K.; Barton, J. K. Direct Electrochemistry of Endonuclease III in the Presence and Absence of DNA. *J. Am. Chem. Soc.* **2006,** *128*, 12082 – 12083.

13) Boon, E. M.; Livingston, A. L.; Chmiel, N. H.; David, S. S.; Barton, J. K. DNA-mediated charge transport for DNA repair. *Proceedings of the National Academy of Sciences* **2003,** *100*, 12543 – 12547.

14) Boal, A. K.; Yavin, E.; Barton, J. K. DNA repair glycosylases with a [4Fe–4S] cluster: A redox cofactor for DNA-mediated charge transport? *Journal of Inorganic Biochemistry* **2007,** *101*, 1913 – 1921.

15) Boon, E. M.; Pope, M. A.; Williams, S. D.; David, S. S.; Barton, J. K. DNA-Mediated Charge Transport as a Probe of MutY/DNA Interaction. *Biochemistry* **2002,** *41*, 8464 – 8470.

16) Solomon, E. I.; Hedman, B.; Hodgson, K. O.; Dey, A.; Szilagyi, R. K. Ligand K-edge X-ray absorption spectroscopy: covalency of ligand–metal bonds *Coord. Chem. Rev.* **2005,** *249*, 97 – 129.

17) Sarangi, R.; George, S. D.; Rudd, D. J.; Szilagyi, R. K.; Ribas, X.; Rovira, C.; Almeida, M.; Hodgson, K. O.; Hedman, B.; Solomon, E. I. Sulfur K-Edge X-ray Absorption Spectroscopy as a Probe of Ligand−Metal Bond Covalency: Metal vs Ligand Oxidation in Copper and Nickel Dithiolene Complexes. *J. Am. Chem. Soc.* **2007,** *129*, 2316 – 2326.

18) Glaser, T.; Rose, K.; Shadle, S. E.; Hedman, B.; Hodgson, K. O.; Solomon, E. I. S K-edge X-ray Absorption Studies of Tetranuclear Iron-Sulfur Clusters: μ-Sulfide Bonding and Its Contribution to Electron Delocalization. *J. Am. Chem. Soc.* **2001,** *123*, 442 – 454.

19) Pheeney, C.G.; Arnold, A.R.; Grodick, M.A.; Barton, J.K. Multiplexed Electrochemistry of DNA-Bound Metalloproteins. *J. Am. Chem. Soc.* **2013**, *135*, 11869 – 11879.

20) Shadle, S. E.; Hedman, B.; Hodgson, K. O.; Solomon, E. I. Ligand K-Edge X-ray Absorption Spectroscopy as a Probe of Ligand-Metal Bonding: Charge Donation and Covalency in Copper-Chloride Systems. *Inorg. Chem.* **1994,** *33*, 4235 – 4244.

21) George, G. N. *EXAFSPAK*, Stanford Synchrotron Radiaton Laboratory: Menlo Park, CA, **1990**.

22) Tenderholt, A. L.; Hedman, B.; Hodgson, K. O. In PySpline: A Modern, Cross-Platform Program for the Processing of Raw Averaged XAS Edge and EXAFS Data, AIP conference Proceedings, **2006**; pp 105 – 107.

23) Frisch, M. J.; Trucks, G. W.; Schlegel, H. B.; Scuseria, G. E.; Robb, M. A.; Cheeseman, J. R.; Scalmani, G.; Barone, V.; Mennucci, B.; Petersson, G. A.; Nakatsuji, H.; Caricato, M.; Li, X.; Hratchian, H. P.; Izmaylov, A. F.; Bloino, J.; Zheng, G.; Sonnenberg, J. L.; Hada, M.; Ehara, M.; Toyota, K.; Fukuda, R.; Hasegawa, J.; Ishida, M.; Nakajima, T.; Honda, Y.; Kitao, O.; Nakai, H.; Vreven, T.; Montgomery, J. A.; Peralta, J. E.; Ogliaro, F.; Bearpark, M.; Heyd, J. J.; Brothers, E.; Kudin, K. N.; Staroverov, V. N.; Kobayashi, R.; Normand, J.; Raghavachari, K.; Rendell, A.; Burant, J. C.; Iyengar, S. S.; Tomasi, J.; Cossi, M.; Rega, N.; Millam, J. M.; Klene, M.; Knox, J. E.; Cross, J. B.; Bakken, V.; Adamo, C.; Jaramillo, J.; Gomperts, R.; Stratmann, R. E.; Yazyev, O.; Austin, A. J.; Cammi, R.; Pomelli, C.; Ochterski, J. W.; Martin, R. L.; Morokuma, K.; Zakrzewski, V.

G.; Voth, G. A.; Salvador, P.; Dannenberg, J. J.; Dapprich, S.; Daniels, A. D.; Farkas; Foresman, J. B.; Ortiz, J. V.; Cioslowski, J.; Fox, D. J. Gaussian 09, Revision B.01. Wallingford CT, **2009**.

24) Fromme, J. C.; Verdine, G. L. Structure of a trapped endonuclease III–DNA covalent intermediate. *EMBO J.* **2003,** *22*, 3461 – 3471.

25) Arnold, A.R.; Barton, J.K. DNA Protection by the Bacterial Ferritin Dps via DNA Charge Transport. *J. Am. Chem. Soc.* **2013**, *135*, 15726 – 15729.

26) Porello, S.L.; Cannon, M.J.; David, S.S. A Substrate Recognition Role for the $[4Fe4S]^{2+}$ Cluster of the DNA Repair Glycosylase MutY. *Biochemistry* **1998**, *37*, 6465 – 6475.

27) Chepanoske, C.L.; Porello, S.L.; Fujiwara, T.; Sugiyama, H.; David, S.S. Substrate Recognition by *Escherichia coli* MutY using Substrate Analogs. *Nucleic Acids Res.* **1999**, *27*, 3197 – 3204.

28) Chmiel, N.H.; Golinelli, M.-P.; Francis, A.W.; David, S.S. Efficient Recognition of Substrates and Substrate Analogs by the Adenine Glycosylase MutY Requires the C-Terminal Domain. *Nucleic Acids Res.* **2001**, *29*, 553 – 564.

29) Bartels, P.L.; Zhou, A.; Arnold, A.R.; Nuñez, N.N.; Crespilho, F.N.; David, S.S.; Barton, J.K. Electrochemistry of the [4Fe4S] Cluster in Base Excision Repair Proteins: Tuning the Redox Potential with DNA. *Langmuir* **2017**, *33*, 2523 – 2530.

30) Hadt, R. G.; Sun, N.; Marshall, N. M.; Hodgson, K. O.; Hedman, B.; Lu, Y.; Solomon, E. I. Spectroscopic and DFT Studies of Second-Sphere Variants of the Type 1 Copper Site in Azurin: Covalent and Nonlocal Electrostatic Contributions to Reduction Potentials. *J. Am. Chem. Soc.* **2012,** *134*, 16701 – 16716.

31) Chepanoske, C. L.; Golinell, M.-P.; Williams, S. D.; David, S. S. Positively Charged Residues within the Iron–Sulfur Cluster Loop of E. coli MutY Participate in Damage Recognition and Removal. *Arch. Biochem. Biophys.* **2000,** *380*, 11 – 19.

32) Kuo, C.-F.; McRee, D. E.; Fisher, C. L.; O'Handley, S. F.; Cunningham, R. P.; Tainer, J. A. Atomic structure of the DNA repair [4Fe-4S] enzyme endonuclease III. *Science* **1992,** *258*, 434 – 440.